Optimal design of rainbow elastic metamaterials

Han Meng[1*], Dimitrios Chronopoulos[1], Adriano T Fabro[2], Ian Maskery[3] and Yanyu Chen[4]

[1]*Institute for Aerospace Technology & The Composites Group, University of Nottingham, NG8 1BB, UK*

[2] *Department of Mechanical Engineering, University of Brasilia, 70910-900, Brazil*

[3]*Centre for Additive Manufacturing, Faculty of Engineering, University of Nottingham, NG8 1BB, UK*

[4]*Department of Mechanical Engineering, University of Louisville, Louisville, KY 40292, USA*

Abstract

In this study, we present an optimization scheme for the resonator distribution in rainbow metamaterials that are constitutive of a Π-shaped beam with parallel plate insertions and two sets of spatially varying cantilever-mass resonators. To improve the vibration attenuation of the rainbow metamaterials at frequencies of interest, two optimization strategies are proposed, aiming at minimizing the maximum and average receptance values respectively. Objective functions for both single and multiple frequency ranges optimization are set up with the frequency response functions predicted by an analytical model. The masses of the two sets of resonators clamped at different side walls of the Π-shaped beams constitute the set of design variables. Optimization functions are solved out with the employment of the Genetic Algorithm method. Dedicate case studies are subsequently conducted to show the feasibility of the proposed scheme. The receptance values are found greatly reduced within the single and multiple optimization frequency ranges. Moreover, it is found that, the maximum

* Corresponding author.
Email: han.meng@nottingham.ac.uk

value based objective function could lead to optimal structures with wider bandgaps but weaker vibration attenuation, while the optimal structure by the average value based objective function has the opposing trend with narrower bandgaps but enhanced vibration attenuation. Objective strategies should be selected according to the application requirements.

Keywords: Rainbow metamaterials, Optimization, Genetic Algorithm, Resonator mass, Multi-frequency ranges

1. Introduction

Metamaterials are artificial constructions that exhibit unique effective properties which cannot be found from conventional materials in nature. In the past decades, attention was first paid to metamaterials to deal with electromagnetic waves [1-4]. Electromagnetic metamaterials possess special negative effective properties such as negative permeability [5] and negative permittivity [6]. Analogically, acoustic/elastic metamaterials tailored to manipulate mechanical waves were developed. The acoustic/elastic metamaterials are composed of fundamental building components and additional mechanical oscillators. Owing to the resonance of oscillators, acoustic/elastic waves inside the acoustic/elastic metamaterials can be altered and favorable properties such as negative effective mass, negative elastic modulus and subwavelength bandgaps emerge.

The very first acoustic metamaterial was realized by Liu *et al.* [7]. They fabricated 3D sonic crystals with periodically arranged spheres that consisted of hard cores and soft coatings. Bandgaps as well as negative effective elastic constants were measured at frequencies where the lattice dimensions were two orders of magnitude smaller than the wavelength. Since then, plenty of acoustic/elastic metamaterials were proposed with various local resonant structures and negative properties. Metamaterials with negative mass/density were most widely mentioned in literature. Yao *et al*. [8, 9], Gao *et al*.[10] and Huang *et al*. [11, 12] investigated negative mass metamaterial structures with idealized mass-spring systems as resonators. Cselyuszka *et al.* [13], Lee *et al.* [14] and Yang *et al.* [15] presented metamaterials containing elastic membranes that had negative mass/density. With regard to negative elastic modulus metamaterials, Fang *et al*. [16], Ding *et al*. [17] and Lee *et al*. [18] created ducts or tubes with Helmholtz resonators which exhibited negative elastic modulus. Except for single negativity, a few

researchers studied metamaterials with double negative properties. Liu *et al*. [19] and Wang [20] developed metamaterials with simultaneous negative mass and negative elastic modulus by introducing springs and rigid bodies with both translational and rotational motions. Ding *et al.* [21] produced double negativity metamaterials with two different kinds of spheres embedded in epoxy matrix. Lee *et al*. [22] investigated double negative metamaterials with the combination of interspaced membranes and side holes. In addition, given the presence of viscoelastic components, dissipative elastic/acoustic metamaterials were also studied extensively. Manimala and Sun [23] developed dissipative mass-in-mass lattice structures containing dashpots with viscous damping. Wang *et al.* [24], Lewinska *et al.* [25] and Krushynska *et al.* [26] investigated dissipative metamaterials that consisted of dense metallic bars with viscoelastic coatings. Xiao *et al.* [27] analyzed the influences of damped mass-spring absorbers on frequency response of laminated acoustic metamaterials. Damping was consequently found through research to reduce peak attenuation but broaden spectrum attenuation. Furthermore, in an effort to develop real-world metamaterials for industrial applications, many researchers focused on metamaterials consisting of engineering structures and local resonators. For typical instance, engineering beams or plates combined with resonators received much attention. Zhang *et al*. [28] and Nouh *et al*. [29] presented metamaterial beams or plates with embedded membrane type resonators. Sugino *et al*. [30], Yu *et al*. [31] and Liu *et al*. [32] investigated the flexural wave attenuation of Euler-Bernoulli beams with local resonators. Li *et al.* [33], Zhang *et al*. [34] and Xiao *et al*. [35] created metamaterials coupling thin plates with different periodically attached resonators.

Apart from a single set of resonators, metamaterials with multiple resonators in a single unit cell were also explored by a limited number of researchers. Peng *et al*. [36],

Pai *et al*. [37], Wang *et al*. [38] and Zhu *et al*. [39] developed metamaterial structures with multiple mass-spring subsystems. Huang and Sun [40] and Chen *et al*. [41] investigated metamaterial lattice structures which contained two mass-in-mass systems in each unit. Li *et al*. [42-45] and Xiao *et al*. [27] designed and optimized various metamaterials with multi-resonators for impact force mitigation. The multiple resonators are found to generate stopbands within multi-frequency ranges.

Most of the proposed metamaterials are periodic structures, either single or multiple resonators were periodically distributed in the metamaterials. Even though the periodic metamaterials can obtain good vibration attenuation within bandgap regions, the width of bandgaps is still narrow for practical applications. Achievement of broad low frequency vibration attenuation remains a challenge for the designing of metamaterials. Sun *et al.* [46] and Pai [47] investigated nonperiodic metamaterial bars or beams with spatially varying resonators as an attempt to enlarge bandgaps. It was found that metamaterials could have better vibration attenuation with properly designed nonperiodic resonators. These design procedures have, however, mainly been based on trial and error, which is unlikely to give optimal designs and possibly leaves large design space unexplored.

We hereby present the first attempt to optimize rainbow structures for maximum noise and vibration absorption within targeted frequency ranges. We first put forward design approaches for the distributions of resonators in nonperiodic metamaterials. These are composed of Π-shaped beams partitioned by plate insertions and spatially varying cantilever mass resonators. The main optimization objective is to maximize the vibration attenuation at frequencies of interest by changing the distributions of rainbow-shaped resonators. To realize the objective, we devise two optimization strategies, including minimizing the maximum and average receptance values at prescribed single

and multi-frequency ranges. Two optimization objective functions are set up based on Frequency Response Functions (FRFs) estimated by an analytical model. Compared with Finite Element (FE) models that are widely applied for the modelling of metamaterials, the analytical model can provide much faster prediction of the FRFs of rainbow metamaterials. Given the FRFs calculation process would be called a great number of times during the optimization process, the analytical model is the only feasible option for the optimization to converge.

A Genetic Algorithm (GA) method is adopted to solve the aforementioned optimization objective functions. GA searches for the optimal results based on natural selection and evolutionary biology theory. Different from other optimization methods, such as gradient-based optimization methods that rely on the derivative calculation and tend to find local optimization results, GA has the ability of finding out reasonable global near-optimal results quickly rather than finding perfect global optimal results that are only partly better with much long time consumed, therefore GA is more suitable for multimodal function models and objectives. In fact, GA has been applied to the optimization of metamaterials by a few researchers. For instance, Dong *et al*. [48, 49] and Gazonas *et al*. [50] presented topology optimization of two-dimensional periodic lattice metamaterials with GA method. The present optimization objective functions are typically nonlinear multi-model functions, thus can be ideally solved by the employment of GA method.

The paper is structured as follows. Section 2 describes the analytical model of the FRFs of the rainbow metamaterials and the experimental validation of the analytical model. In Section 3 two objective functions are set up considering maximum and average receptance values within the prescribed frequency ranges. After that, the GA method is introduced in Section 4 to solve the objective functions. Optimization

examples are proposed in Section 5 to show the feasibility of the employed approaches. Finally, the main conclusions and further perspectives are summarized in Section 6.

2. Analytical predictions of the FRFs of rainbow metamaterials

An analytical model is first developed in this section to estimate the FRFs of the proposed metamaterials. The analytical model is later verified by experimental results. Optimization objective functions will be set up based on the proposed analytical model in the following sections.

The metamaterial is composed of a Π-shaped beam partitioned by parallel plate insertions as backbones and cantilever-mass resonators as shown Figs. 1(a)-(c). Two cantilever-mass resonators are connected to the side walls of the Π-shaped beam inside each substructure. The cantilever-mass resonators show spatial variation along the *x*-axis of the Π-shaped beam. The structure can exhibit single or multi-frequency bandgaps depending on whether the two sets of resonators attached to different side walls are symmetric.

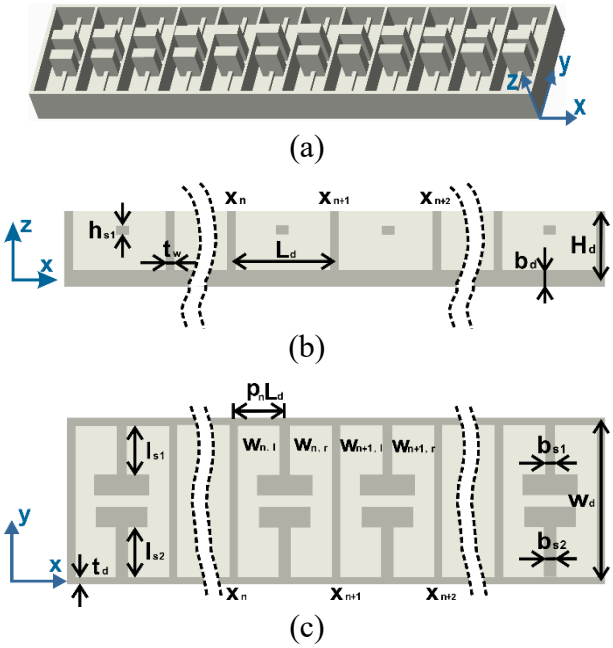

Fig. 1 Schematic diagram of the rainbow metamaterial (a) side view, (b) global view, (c) top view

Based on the theory of elasticity, displacements of the nth and $(n+1)$th segments of the Π-shaped beam as shown in Fig. 1(b) can be written as

$$W_{n,l} = \alpha_{n,l}\mathrm{e}^{-\mathrm{j}k(x-x_n)} + \beta_{n,l}\mathrm{e}^{-k(x-x_n)} + \chi_{n,l}\mathrm{e}^{\mathrm{j}k(x-x_n)} + \varepsilon_{n,l}\mathrm{e}^{k(x-x_n)}, \tag{1}$$

$$W_{n,r} = \alpha_{n,r}\mathrm{e}^{-\mathrm{j}k(x-(x_n+p_nL_d))} + \beta_{n,r}\mathrm{e}^{-k(x-(x_n+p_nL_d))} + \chi_{n,r}\mathrm{e}^{\mathrm{j}k(x-(x_n+p_nL_d))} + \varepsilon_{n,r}\mathrm{e}^{k(x-(x_n+p_nL_d))}, \tag{2}$$

$$W_{n+1,l} = \alpha_{n+1,l}\mathrm{e}^{-\mathrm{j}k(x-x_{n+1})} + \beta_{n+1,l}\mathrm{e}^{-k(x-x_{n+1})} + \chi_{n+1,l}\mathrm{e}^{\mathrm{j}k(x-x_{n+1})} + \varepsilon_{n+1,l}\mathrm{e}^{k(x-x_{n+1})}, \tag{3}$$

$$W_{n+1,r} = \alpha_{n+1,r}\mathrm{e}^{-\mathrm{j}k(x-(x_{n+1}+p_{n+1}L_d))} + \beta_{n+1,r}\mathrm{e}^{-k(x-(x_{n+1}+p_{n+1}L_d))} + \chi_{n+1,r}\mathrm{e}^{\mathrm{j}k(x-(x_{n+1}+p_{n+1}L_d))} + \varepsilon_{n+1,r}\mathrm{e}^{k(x-(x_{n+1}+p_{n+1}L_d))}, \tag{4}$$

where j is the imaginary unit, $W_{i,l}$ and $W_{i,r}$ $(i=1,2,...)$ are the displacements before and after the resonators of the ith segments respectively, x_i $(i=1,2,...)$ is the position of the ith plate insertion in x direction, $k=(\rho A/EI_z)^{1/4}\sqrt{\omega}$, A and I_z are the cross section area and second moment of area of the Π-shaped beam respectively, ρ is the density of the structure, $E=E_0(1+\mathrm{j}\eta)$, E_0 and η are the Young's modulus and loss factor of the material respectively. Moreover, L_d is the distance between parallel plate insertions and p_iL_d $(i=1,2,...)$ represents the locations of resonators inside the ith segment of the metamaterial beam.

Given the continuities of displacement, slope, bending moment and shearing force inside the segment, displacements before and after the resonators of the nth segment are related by

$$\begin{aligned} W_{n,l}\big|_{x=x_n+p_nL_d} &= W_{n,r}\big|_{x=x_n+p_nL_d} \\ W'_{n,l}\big|_{x=x_n+p_nL_d} &= W'_{n,r}\big|_{x=x_n+p_nL_d} \\ W''_{n,l}\big|_{x=x_n+p_nL_d} &= W''_{n,r}\big|_{x=x_n+p_nL_d} \\ EI_z W'''_{n,l}\big|_{x=x_n+p_nL_d} + F_n &= EI_z W'''_{n,r}\big|_{x=x_n+p_nL_d} \end{aligned}, \tag{5}$$

where F_i $(i=1,2,...)$ is the interaction force between the two resonators and the Π-shaped beam inside the ith segment. The calculation process of F_i is given in detail

within the Appendix.

Substituting Eqs. (1) and (2) into (5), arrives

$$\left[\alpha_{n,r},\beta_{n,r},\chi_{n,r},\varepsilon_{n,r}\right]^{\mathrm{T}}=\mathbf{R}_c{}^{-1}\mathbf{R}_n\mathbf{\Lambda}_{n,l}\left[\alpha_{n,l},\beta_{n,l},\chi_{n,l},\varepsilon_{n,l}\right]^{\mathrm{T}},\tag{6}$$

where the matrices $\mathbf{R}_c$, $\mathbf{R}_n$ and $\mathbf{\Lambda}_{n,l}$ are given as

$$\mathbf{R}_c=\begin{bmatrix}1 & 1 & 1 & 1\\ -\mathrm{j} & -1 & \mathrm{j} & 1\\ -1 & 1 & -1 & 1\\ \mathrm{j}EI_z k^3 & -EI_z k^3 & -\mathrm{j}EI_z k^3 & EI_z k^3\end{bmatrix}$$

$$\mathbf{R}_n=\begin{bmatrix}1 & 1 & 1 & 1\\ -\mathrm{j} & -1 & \mathrm{j} & 1\\ -1 & 1 & -1 & 1\\ \left(\mathrm{j}EI_z k^3+N_{s,n}\right) & \left(-EI_z k^3+N_{s,n}\right) & \left(-\mathrm{j}EI_z k^3+N_{s,n}\right) & \left(EI_z k^3+N_{s,n}\right)\end{bmatrix}.\tag{7}$$

$$\mathbf{\Lambda}_{n,l}=\mathrm{diag}\left(\mathrm{e}^{-\mathrm{j}kp_nL_d},\mathrm{e}^{-kp_nL_d},\mathrm{e}^{\mathrm{j}kp_nL_d},\mathrm{e}^{kp_nL_d}\right)$$

Besides, the parallel plate insertions can be modeled as added mass to the Π-shaped beam. Thus, considering the continuities of displacement, slope and equilibrium conditions of the plate insertions, the displacement relationship between the nth and $(n+1)$th segments can be written as

$$\begin{aligned}W_{n,r}\big|_{x=x_{n+1}}&=W_{n+1,l}\big|_{x=x_{n+1}}\\ W'_{n,r}\big|_{x=x_{n+1}}&=W'_{n+1,l}\big|_{x=x_{n+1}}\\ EI_z W''_{n,r}\big|_{x=x_{n+1}}-J_f\omega^2 W'_{n,r}\big|_{x=x_{n+1}}&=EI_z W''_{n+1,l}\big|_{x=x_{n+1}}\\ EI_z W'''_{n,r}\big|_{x=x_{n+1}}+m_f\omega^2 W_{n,r}\big|_{x=x_{n+1}}&=EI_z W'''_{n+1,l}\big|_{x=x_{n+1}}\end{aligned},\tag{8}$$

where m_f and J_f are the mass and moment of inertia of the plate insertions.

Substituting Eqs. (2) and (3) into Eq. (8), yields,

$$\left[\alpha_{n+1,l},\beta_{n+1,l},\chi_{n+1,l},\varepsilon_{n+1,l}\right]^{\mathrm{T}}=\mathbf{R}^{-1}\mathbf{U}\mathbf{\Lambda}_{n,r}\left[\alpha_{n,r},\beta_{n,r},\chi_{n,r},\varepsilon_{n,r}\right]^{\mathrm{T}},\tag{9}$$

where $\mathbf{R}$, $\mathbf{U}$ are

$$\mathbf{\Lambda}_{n,r}=\mathrm{diag}\left(\mathrm{e}^{-\mathrm{j}k(1-p_n)L_d},\mathrm{e}^{-k(1-p_n)L_d},\mathrm{e}^{\mathrm{j}k(1-p_n)L_d},\mathrm{e}^{k(1-p_n)L_d}\right)$$

$$\mathbf{R}=\begin{bmatrix}1 & 1 & 1 & 1\\ -\mathrm{j} & -1 & \mathrm{j} & 1\\ -EI_zk^2 & EI_zk^2 & -EI_zk^2 & EI_zk^2\\ \mathrm{j}EI_zk^3 & -EI_zk^3 & -\mathrm{j}EI_zk^3 & EI_zk^3\end{bmatrix} \quad .(10)$$

$$\mathbf{U}=\begin{bmatrix}1 & 1 & 1 & 1\\ -\mathrm{j} & -1 & \mathrm{j} & 1\\ \left(-EI_zk^2+\mathrm{j}J_f\omega^2k\right) & \left(EI_zk^2+J_f\omega^2k\right) & \left(-EI_zk^2-\mathrm{j}J_f\omega^2k\right) & \left(EI_zk^2-J_f\omega^2k\right)\\ \left(\mathrm{j}EI_zk^3+m_f\omega^2\right) & \left(-EI_zk^3+m_f\omega^2\right) & \left(-\mathrm{j}EI_zk^3+m_f\omega^2\right) & \left(EI_zk^3+m_f\omega^2\right)\end{bmatrix}$$

Combing Eq. (6) with (9), the displacement transfer matrix between two segments is derived as

$$\begin{aligned}&\left[\alpha_{n+1,l},\beta_{n+1,l},\chi_{n+1,l},\varepsilon_{n+1,l}\right]^{\mathrm{T}}=\mathbf{T}_n\left[\alpha_{n,l},\beta_{n,l},\chi_{n,l},\varepsilon_{n,l}\right]^{\mathrm{T}}\\ &=\mathbf{T}_n\mathbf{T}_{n\text{-}1}\cdots\mathbf{T}_1\left[\alpha_{1,l},\beta_{1,l},\chi_{1,l},\varepsilon_{1,l}\right]^{\mathrm{T}}\end{aligned}, \quad (11)$$

where $\mathbf{T}_n=\mathbf{R}^{-1}\mathbf{U}\mathbf{\Lambda}_{n,r}\mathbf{R}_c^{-1}\mathbf{R}_n\mathbf{\Lambda}_{n,l}$.

Assuming a finite rainbow metamaterial is excited at one end by a force F, the equilibrium equations at the two ends are written as

$$\begin{aligned}F+m_f\omega^2W_{1,l}\big|_{x=0}&=EI_zW_{1,l}'''\big|_{x=0}\\ -J_f\omega^2W_{1,l}'\big|_{x=0}&=EI_zW_{1,l}''\big|_{x=0}\\ EI_zW_{q,r}'''\big|_{x=L}+m_f\omega^2W_{q,r}\big|_{x=L}&=0\\ EI_zW_{q,r}''\big|_{x=L}-J_f\omega^2W_{q,r}'\big|_{x=L}&=0\end{aligned}, \quad (12)$$

where q is the number of segments of the Π-shaped beam, $L=qL_d$ is the length of the metamaterial beam. According to Eqs. (9), (11) and (12), the displacement at the end of the metamaterial beam can be derived as

$$W_{q,r}\big|_{x=L}=\alpha_{q,r}\mathrm{e}^{-\mathrm{j}k(1-p_s)L_d}+\beta_{q,r}\mathrm{e}^{-k(1-p_s)L_d}+\chi_{q,r}\mathrm{e}^{\mathrm{j}k(1-p_s)L_d}+\varepsilon_{q,r}\mathrm{e}^{k(1-p_s)L_d}, \quad (13)$$

where

$$\left[\alpha_{q,r},\beta_{q,r},\chi_{q,r},\varepsilon_{q,r}\right]^{\mathrm{T}}=\mathbf{\Pi}\mathbf{\Psi}^{-1}\left[0,F,0,0\right]^{\mathrm{T}}$$

$$\mathbf{\Psi}=\left[\mathbf{\Psi}_1,\mathbf{\Psi}_2\right]^{\mathrm{T}}$$

$$\mathbf{\Psi}_1=\begin{bmatrix}\left(-EI_z k^2-\mathrm{j}kJ_f\omega^2\right) & \left(EI_z k^2-kJ_f\omega^2\right) & \left(-EI_z k^2+\mathrm{j}kJ_f\omega^2\right) & \left(EI_z k^2+kJ_f\omega^2\right)\\ \left(\mathrm{j}EI_z k^3-m_f\omega^2\right) & \left(-EI_z k^3-m_f\omega^2\right) & \left(-\mathrm{j}EI_z k^3-m_f\omega^2\right) & \left(EI_z k^3-m_f\omega^2\right)\end{bmatrix} \quad .(14)$$

$$\mathbf{\Psi}_2=\begin{bmatrix}\left(-EI_z k^2+\mathrm{j}J_f\omega^2 k\right) & \left(EI_z k^2+J_f\omega^2 k\right) & \left(-EI_z k^2-\mathrm{j}J_f\omega^2 k\right) & \left(EI_z k^2-J_f\omega^2 k\right)\\ \left(\mathrm{j}EI_z k^3+m_f\omega^2\right) & \left(-EI_z k^3+m_f\omega^2\right) & \left(-\mathrm{j}EI_z k^3+m_f\omega^2\right) & \left(EI_z k^3+m_f\omega^2\right)\end{bmatrix}\mathbf{\Lambda}_{q,r}\mathbf{\Pi}$$

Finally, the receptance function of the rainbow metamaterial can be calculated by

$$R_{ec}=20\log_{10}\left|\frac{W_{q,r}\big|_{x=L}}{F}\right|. \quad (15)$$

The analytical model is validated by comparison with experimental results below. Three rainbow metamaterials are manufactured by Additive Manufacturing (AM) technology with Nylon-12 powder. The Nylon-12 powder is sintered layer by layer to predesigned shapes with the laser as a power source, the manufacturing process is known as Selective Laser Sintering (SLS) method. SLS is one of the most popular AM technologies. Compared with other popular AM technologies such as Stereolithography and Fused Deposition Modeling, the SLS method requires no molds or additional supporting materials during the printing process, hence highly suitable for the fabrication of complex and delicate objects. The density of the printed structures is 930 kg/m^3, average flexural modulus is 1.8 GPa, Poisson's ratio is 0.3, and the loss factor is 0.03. The density of the samples was obtained by the ratio of mass to volume, while the flexural modulus was determined by following the standard three-point bending method with standard specimens printed by the same material and SLS method. The geometrical parameters of the samples are listed in Table 1.

Table 1 Geometrical parameters of the printed rainbow metamaterials

Π-shaped beam and plate insertions

Height	$H_d = 10$ mm
Width	$w_d = 51$ mm
Side wall thickness	$t_d = 2$ mm
Backplate thickness	$b_d = 5$ mm
Plate insertion thickness	$t_w = 2$ mm
Distance between plate insertion	$L_d = 15$ mm
Number of segments	$q = 17$
Total length of metamaterial beams	$L = 0.255$ m

Cantilever beam

Sample 1#, Sample 2#

Height	$h_{s1} = h_{s2} = 1.4$ mm
Width	$b_{s1} = b_{s2} = 1.9$ mm
Length	$l_{s1} = l_{s2} = 21.2$ mm

Sample 3#

Height	$h_{s1} = 1.4$ mm, $h_{s2} = 2.3$ mm
Width	$b_{s1} = 1.9$ mm, $b_{s2} = 2.3$ mm
Length	$l_{s1} = l_{s2} = 21.2$ mm

The FRF measuring system for the printed metamaterial beams is schematically illustrated in Fig. 2. The printed structures are excited at one end by a mechanical shaker (Modal Shop 2060E) as shown in Fig. 3. A signal source is first generated by the computer, which goes through the junction box (Polytec VIB-E-400) and is amplified later (Modal Shop 2050E09 amplifier). The signal source determines the excitation frequency, amplitude and waveform of the input force of the shaker. An impedance head (PCB 288D01) is attached to the excitation point of the structures to measure the actual input forces. The displacements of the other end of metamaterial beam are measured by a Doppler laser vibrometer (Polytec PDV-100), and are later sent to the junction box and the computer. When the computer receives information of the actual excitation

force and structure displacements, FRFs can be computed.

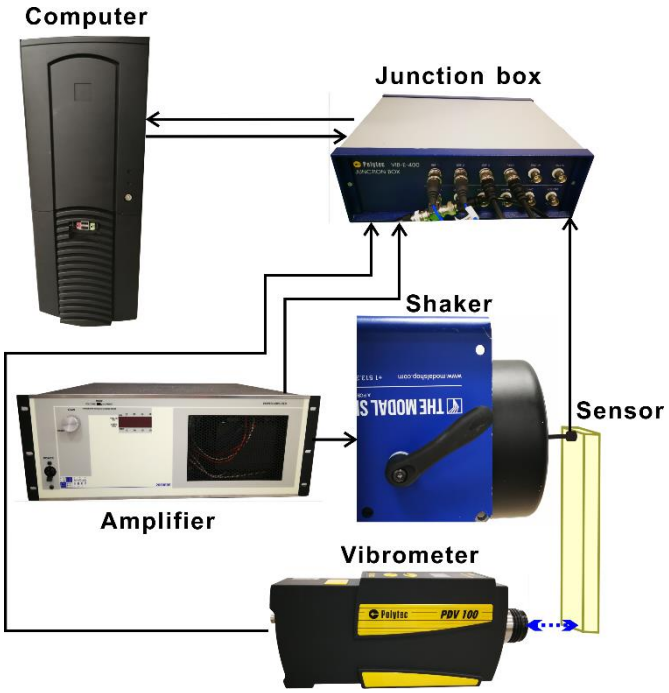

Fig. 2 Schematic diagram of the FRFs testing system

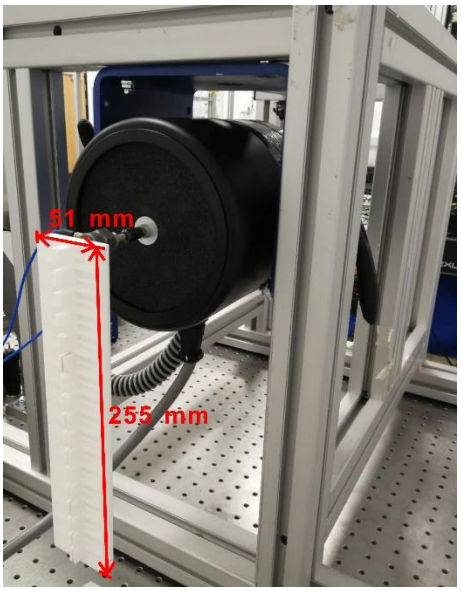

Fig. 3 Experimental setup of the tested beam and mechanical shaker

Comparison between analytical and experimental results are shown in Figs. 4(a)-(c). The resonator distributions of the metamaterial beams are also shown in the Figs. 4(a)-(c). It is noted that m_{1i} and m_{2i} $(i=1,2,...,q)$ represent the mass of the two sets of resonators attached at different side walls of the Π-shaped beam. The reference mass

m_r denotes unit mass of the Π-shaped beam with parallel plate insertions, as

$$m_r = M / q, \tag{16}$$

where M is the total mass of the metamaterial beam.

It can be seen from Figs. 4(a)-(c) that the analytical results agree well with experimental results. Sample 1# and Sample 2# have symmetric resonators, thus single bandgap can be seen from both experimental and analytical curves in Figs. 4(a)-(b). Sample 3# has non-symmetric resonators, two bandgaps appear in both the analytical and experimental results as shown in Fig. 4(c). The differences between the experimental and analytical results are mainly the bandgap frequencies, which might be caused by the uncertainties of experimental conditions and 3D manufacturing process. Especially, the dimension and physical parameter variabilities introduced by the 3D printing process are found to have greatly influenced the FRFs of rainbow metamaterial [51], which will be explored specifically in further work.

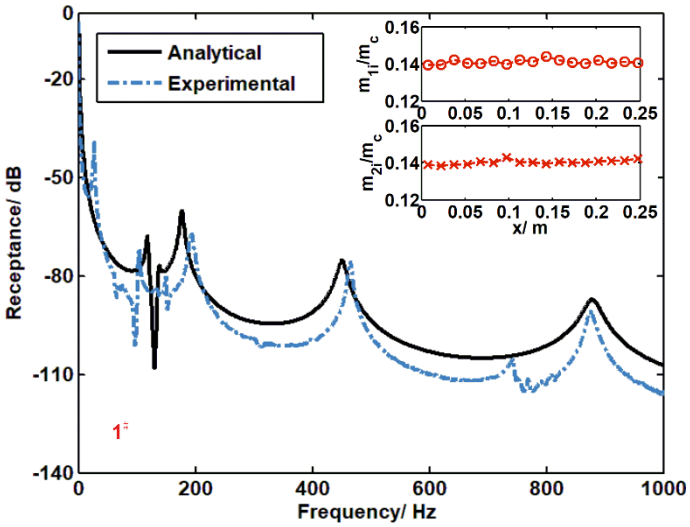

(a)

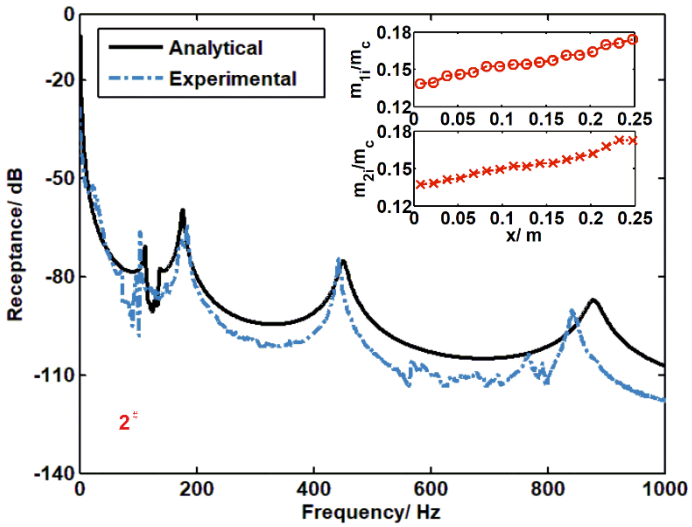

(b)

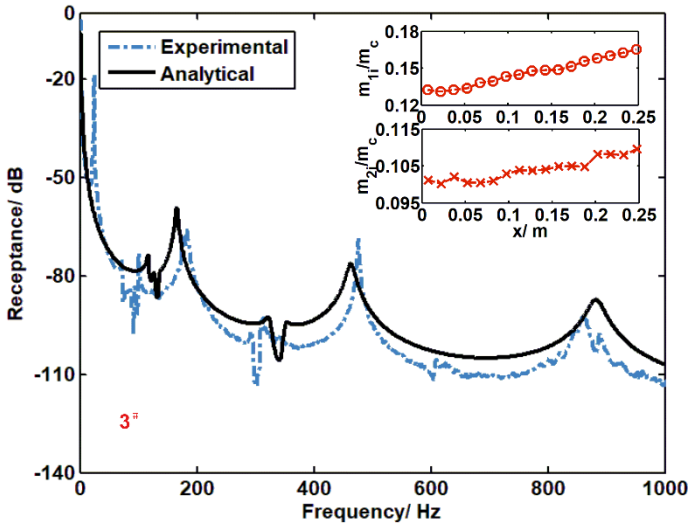

(c)

Fig. 4 Receptance value comparison between the analytical (——)and experimental (- - -) results (a) Sample 1#, (b) Sample 2#, (c) Sample 3#. The mass distributions of two sets of resonators are shown in the subfigures.

3. Optimization strategy

The main optimization objective of the present study is to achieve effective vibration attenuation at frequencies of interest. As discussed in the last section, the FRFs of the rainbow metamaterials are closely related to the distributions of resonators, we therefore assign the mass of spatially varying resonators as design variables. In addition, since the rainbow metamaterial can possess multi-frequency bandgaps with non-

symmetric resonators as shown in Fig. 4(c), symmetric as well as non-symmetric rainbow-shaped resonators are considered in the optimization strategies for the purpose of obtaining both single and multi-frequency vibration attenuation.

3.1 Optimization for a single prescribed frequency range

To maximize the vibration attenuation in a prescribed frequency range, two optimization strategies are proposed that invoke two objective functions respectively. The objective functions can be defined based on maximum receptance value or average receptance value within the prescribed frequency range.

3.1.1 Maximum value based objective function

Receptance values within the prescribed frequency range are expected to be small when their maximum value remains low. Therefore, searching for the distribution of resonators that can minimize the maximum receptance value is naturally a method of optimizing the vibration attenuation within the prescribed frequency range.

The optimization objective function that is based on the maximum receptance value within the prescribed frequency ranges, can be given as

$$\min \quad \max\left(R_{ec}\left(\mathbf{M}_1, \mathbf{M}_2, \mathbf{\Phi}\right)\right), \tag{17}$$

where the receptance function R_{ec} is calculated by Eq. (15), $\mathbf{\Phi} = \left(f_1 \sim f_2\right)$ represents the prescribed frequency regime. The matrices $\mathbf{M}_1 = \left(m_{11}, m_{12}, ..., m_{1q}\right)$ and $\mathbf{M}_2 = \left(m_{21}, m_{22}, ..., m_{2q}\right)$ represent the mass of the two sets of resonators, $\mathbf{M}_1$ is assumed to be equal to $\mathbf{M}_2$ for the single frequency range optimization.

The mass of each resonator cannot be less than zero. Besides, the total mass of the resonators cannot be overweight for the sake of maintaining the dynamic stability of the metamaterial beam and being favorable for engineering applications. Here we assume that the upper limit of total resonator mass to the mass of the whole

metamaterial beam is 30%. Constrains of the design variables are hence given as,

$$\begin{aligned} s.t.\quad & m_{1i}=m_{2i} \\ & m_{11}, m_{12}, ..., m_{1q} \geq 0 \\ & 2\sum_i m_{1i} \leq 0.3M \\ & i=1,2,...,q \end{aligned} . \tag{18}$$

In addition, the mass of each resonator could be any value between $0 \sim 0.3M$ technically, nonetheless, to make the resonator mass change naturally and the optimization trends easily to be cognized and utilized in applications, we use a sinusoidal function to express resonator mass distributions,

$$m_{1i} = A+B\sin\left(Cx_{mi}+D\right) \quad i=1,2,...,q\,, \tag{19}$$

where $x_{mi}=x_i+p_iL_d$ $\left(i=1,2,...,q\right)$ represents the position of m_{1i} and m_{2i} in x direction. In principle, more complex distributions can be also piled up based on simple sinusoidal functions.

Substituting Eq. (19) into Eq. (18), the design variables are altered from each resonator mass to the 4 unknown parameters $A,\ B,\ C,\ D$ in the sinusoidal function, the constrains are finally given as

$$\begin{aligned} s.t.\quad & A+B\sin\left(Cx_{mi}+D\right) \geq 0 \\ & 2\sum_i \left(A+B\sin\left(Cx_{mi}+D\right)\right) \leq 0.3M \\ & 0 \leq Cx_{mi}+D \leq 2\pi \\ & i=1,2,...,q \end{aligned} . \tag{20}$$

3.1.2 Average value based objective function

The average value is another evident indicator of receptance value quality within a prescribed frequency range, therefore, another optimization objective function can be set up based on the average receptance value within the prescribed frequency range,

$$\min \quad \frac{\int_{\mathbf{\Phi}} R_{ec}\left(A,B,C,D,\mathbf{\Phi}\right)\mathrm{d}f}{f_2-f_1} . \tag{21}$$

However, the integral is usually hard computationally expensive to achieve for complex receptance function as defined by Eq. (15) but, the integral can be mathematically approximated by

$$\int_{\mathbf{\Phi}} R_{ec}\left(A,B,C,D,\mathbf{\Phi}\right)\mathrm{d}f \approx \sum_{\mathbf{\Phi}} R_{ec}\left(A,B,C,D,\mathbf{\Phi}\right)\Delta f\ , \tag{22}$$

where Δf denotes the frequency step.

The optimization objective function hence becomes

$$\min\ \frac{\sum_{\mathbf{\Phi}} R_{ec}\left(A,B,C,D,\mathbf{\Phi}\right)\Delta f}{f_2 - f_1}. \tag{23}$$

The constrains of the design variables defined by Eq. (20) are similarly applicable to the average value based optimization objective function.

3.2 Optimization for prescribed multi-frequency ranges

Similar to the single frequency optimization, two objective functions are proposed by virtue of either maximum or average receptance values for the prescribed multi-frequency range optimization. The maximum or average receptance value of each frequency range can be involved in the objective functions by adding weighted parameters.

3.2.1 Maximum value based objective function

The objective function based on maximal receptance values of multi-frequency ranges can be written as,

$$\min\ \left[\max\left(R_{ec}\left(\mathbf{M}_1,\mathbf{M}_2,\mathbf{\Phi}_1\right)\right),\max\left(R_{ec}\left(\mathbf{M}_1,\mathbf{M}_2,\mathbf{\Phi}_2\right)\right)\right]\left[v_1,\left(1-v_1\right)\right]^{\mathrm{T}}, \tag{24}$$

where $\mathbf{\Phi}_1=\left(f_{11}\sim f_{12}\right)$ and $\mathbf{\Phi}_2=\left(f_{21}\sim f_{22}\right)$ represent the two prescribed frequency ranges. It is noted that $\left[v_1,\left(1-v_1\right)\right]^{\mathrm{T}}$ $\left(0\le v_1\le 1\right)$ denotes the weighted parameters of the two frequency ranges. The weighted parameters can be set as equal or unequal values to emphasize the equal importance of both frequency ranges or the priority of

one frequency range over the other one for specific vibration control purposes. The two sets of resonators are in the general case non-symmetric for the multi-frequency vibration attenuation.

The constrains of the design variables are given as:

$$\begin{aligned} s.t.\quad & m_{11}, m_{12}, ..., m_{1q} \geq 0 \\ & m_{21}, m_{22}, ..., m_{2q} \geq 0 \\ & \sum_i \left(m_{1i} + m_{2i} \right) \leq 0.3M \\ & i = 1, 2, ..., q \end{aligned} . \tag{25}$$

As discussed in the last subsection, sinusoidal functions are employed to express the distributions of resonating masses

$$\begin{aligned} m_{1i} &= A_1 + B_1 \sin\left(C_1 x_{mi} + D_1 \right) \quad i = 1, 2, ..., q \\ m_{2i} &= A_2 + B_2 \sin\left(C_2 x_{mi} + D_2 \right) \quad i = 1, 2, ..., q \end{aligned} . \tag{26}$$

Therefore, the constraints for the multi-frequency range optimization can be given as

$$\begin{aligned} s.t.\quad & A_1 + B_1 \sin\left(C_1 x_{mi} + D_1 \right) \geq 0 \\ & A_2 + B_2 \sin\left(C_2 x_{mi} + D_2 \right) \geq 0 \\ & \sum_i \left(A_1 + B_1 \sin\left(C_1 x_{mi} + D_1 \right) + A_2 + B_2 \sin\left(C_2 x_{mi} + D_2 \right) \right) \leq 0.3M \\ & 0 \leq C_1 x_{mi} + D_1 \leq 2\pi \\ & 0 \leq C_2 x_{mi} + D_2 \leq 2\pi \\ & i = 1, 2, ..., q \end{aligned} . \tag{27}$$

3.2.2 Average value based objective function

Similarly, the average receptance objective function to be optimized is given with weighted parameters, as

$$\min \quad \left\{ \left[\frac{\int_{\mathbf{\Phi}_1} R_{ec}\left(\mathbf{M}_1, \mathbf{M}_2, \mathbf{\Phi}_1 \right) \mathrm{d}f}{f_{12} - f_{11}}, \frac{\int_{\mathbf{\Phi}_2} R_{ec}\left(\mathbf{M}_1, \mathbf{M}_2, \mathbf{\Phi}_2 \right) \mathrm{d}f}{f_{22} - f_{21}} \right] \left[v_1, \left(1 - v_1 \right) \right]^{\mathrm{T}} \right\}. \tag{28}$$

The integrals of receptance values can be approximated by

$$\min \quad \left\{ \left[\frac{\sum_{\mathbf{\Phi}_1} R_{ec}\left(\mathbf{M}_1, \mathbf{M}_2, \mathbf{\Phi}_1\right) \Delta f}{f_{12} - f_{11}}, \frac{\sum_{\mathbf{\Phi}_2} R_{ec}\left(\mathbf{M}_1, \mathbf{M}_2, \mathbf{\Phi}_2\right) \Delta f}{f_{22} - f_{21}} \right] \left[v_1, \left(1 - v_1\right) \right]^{\mathrm{T}} \right\}. \quad (29)$$

The constrains of design variables are identical to that described by Eq. (27).

4. GA optimization method

The proposed objective functions are complex multimodal functions as shown in the Appendix. A GA method is employed to solve the aforementioned objective functions. The GA optimization method starts with the creation of an initial population of chromosomes. Multiple individuals exist in each generation. Fitness functions are set up to evaluate the quality of each individual. For the optimization problem mentioned above, objective functions defined by Eqs. (17), (23), (24) and (29) can be set as 4 fitness functions. Subsequently, fitness values of individuals are estimated by the corresponding fitness functions. If the fitness values satisfy the exit conditions, the optimization process ends, otherwise, the reproduction starts. The termination conditions can be set as average changes in the best fitness values less to be inferior to a customized value. Offspring that are subjected to constraint conditions in Eqs. (20),(27) are reproduced by three methods, namely selection, crossover and mutation. With the process of selection, individuals with better fitness values are selected so that they can transfer their genes to next generations. Afterwards, offspring is generated by the mating of two ‘parents’, namely crossover. Furthermore, the genes of the offspring are also stochastically changed with the process of mutation. After these three reproductions steps, fitness values of new generation are re-evaluated and guides the development of the population. Iterations of the abovementioned GA optimization loop may be repeated hundreds of times to find the optimal results. Figure 5 presents a brief flowchart of the GA optimization process.

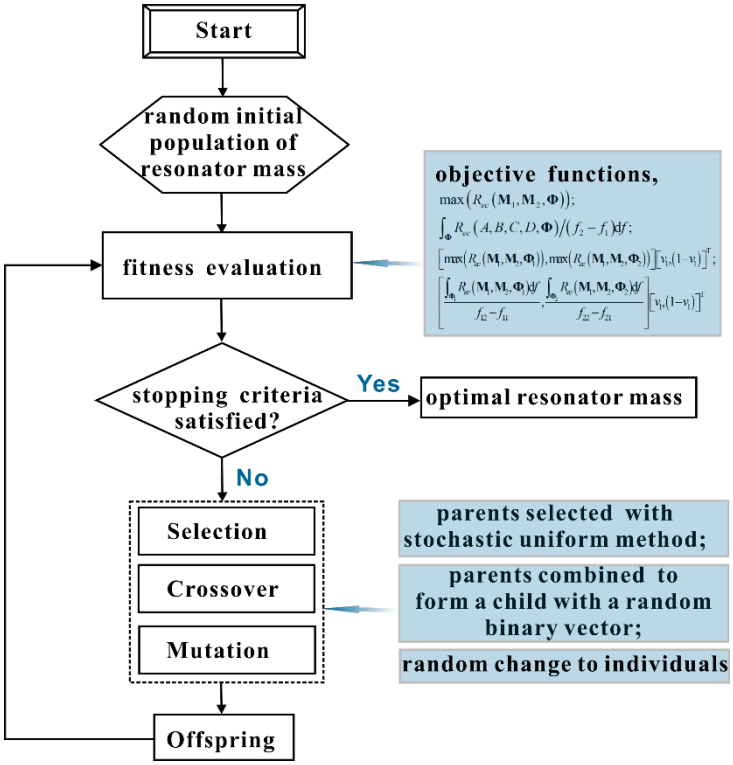

Fig. 5 Flow diagram of GA optimization process for the rainbow metamaterials

5. Optimization examples

In this section, optimization examples are presented to validate the feasibility of the proposed strategies. Optimization results for single and multiple prescribed frequency ranges are discussed respectively in Secs. 5.1 and 5.2. The optimized structures are assumed to have the same physical parameters as the tested samples shown in the last section. The geometrical parameters of Π-shaped beams and cantilever beams of the optimized structures are also the same as that listed in Table 1.

5.1 Single prescribed frequency range optimization

The prescribed single frequency range is assumed as $\mathbf{\Phi}$=140~160 Hz . As discussed in Sec. 3, two objective functions based on maximum and average receptance values are defined for the single frequency optimization. By substituting the objective and constrain functions into the GA process depicted in Fig.5, the optimal results can be figured out.

The best fitness values of each generation during the optimization process by the

two objective functions are shown in Figs. 6 and 8 respectively. It can be seen from Figs. 6 and 8 that the best fitness values decrease gradually with the increase of generation, which means the receptance value inside this frequency range declines with the optimization process. The process stops when the fitness value presents insignificant changes.

The optimal parameters for the maximum-value based objective function are obtained as

$$\begin{aligned} & m_{1i} = m_{2i} = A + B\sin\left(Cx_{mi} + D\right) \quad i = 1, 2, ..., q \\ & A = 0.067353 m_r \\ & B = 0.019595\ m_r \\ & C = -3.94685 \\ & D = -0.41671 \end{aligned} \tag{30}$$

Meanwhile, the optimization results for the average-value based objective function are computed as

$$\begin{aligned} & m_{1i} = m_{2i} = A + B\sin\left(Cx_{mi} + D\right) \quad i = 1, 2, ..., q \\ & A = 0.038142\ m_r \\ & B = -0.015173 m_r \\ & C = 6.17016 \\ & D = -2.35621 \end{aligned} \tag{31}$$

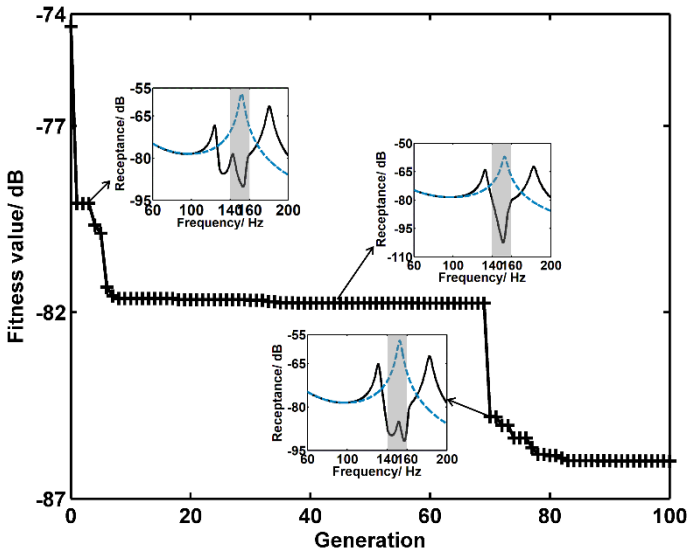

Fig. 6 The evalution history of the best fitness value of each generation during the

single frequency range optimization process with the maximum receptance value based objective function. Receptance values comparison between three rainbow metamaterial beams (——) in the optimization process and no-resonator Π-shaped beams (- - -) of the same mass are shown in the three subfigures.

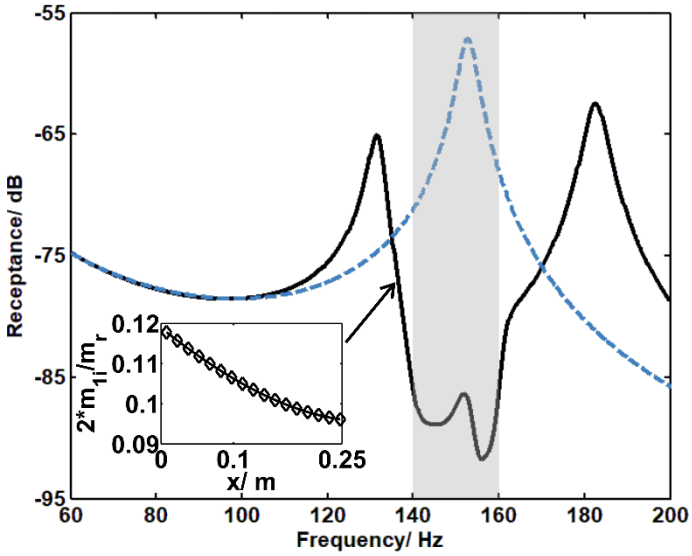

Fig. 7 Receptance value comparison between optimal rainbow metamaterial beam (——) by maximal receptance value based objective function and no-resonator Π-shaped beam (- - -) of the same mass. The resonator mass of the optimal beam is plotted in the subfigure.

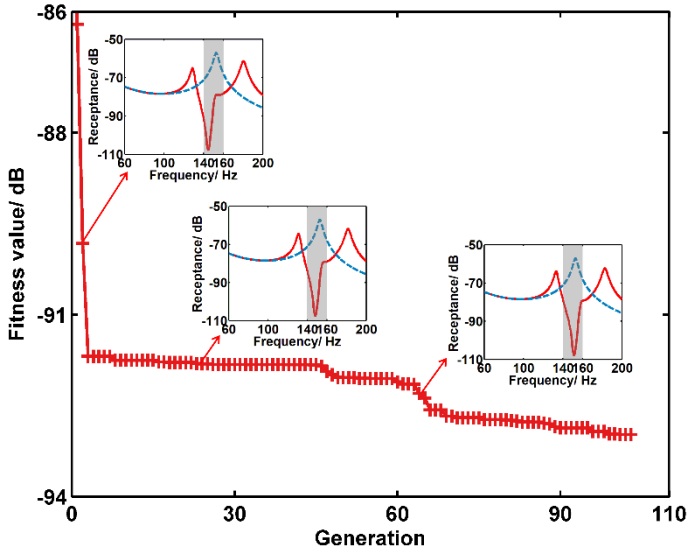

Fig. 8 The evalution history of the best fitness value of each generation during the single frequency range optimization process with the average receptance value based

objective function. Receptance values comparison between three rainbow metamaterial beams (——) in the optimization process and no-resonator Π-shaped beams (- - -) of the same mass are shown in the three subfigures.

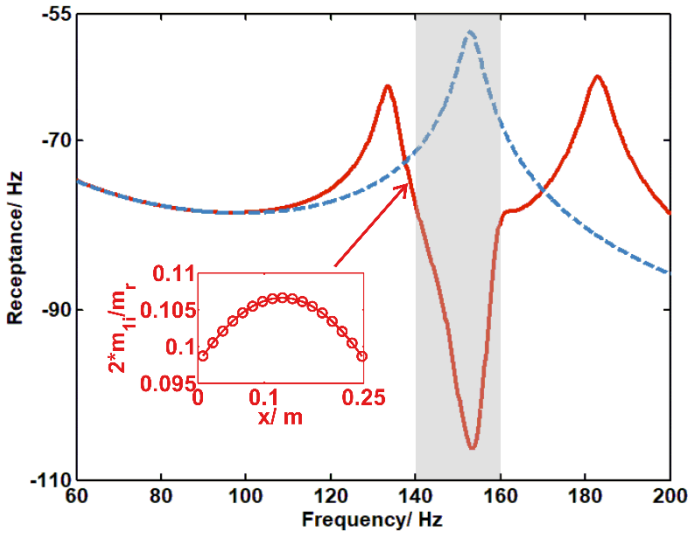

Fig. 9 Receptance value comparison between optimal rainbow metamaterial beam (——) by average receptance value based objective function and no-resonator Π-shaped beam (- - -) of the same mass. The resonator mass of the optimal beam is plotted in the subfigure.

To show the effects of GA optimization clearly, the receptance values of the two optimal metamaterial beams are also compared with that of Π-shaped beam and plate insertions of the same mass but without resonators in Figs. 7 and 9 respectively. It can be seen from Figs. 7 and 9 that both optimal metamaterial beams have bandgaps within the prescribed frequency range, the vibration attenuation is thus greatly enhanced. The optimal rainbow metamaterial beam obtained by maximum-value based objective function has a maximum receptance value that is 28.9 dB less than that of the no-resonator complex beam of the same mass within 140~160 Hz as shown in Fig. 7, while the optimal rainbow metamaterial beam obtained by the average-value based objective function possess an average receptance value with a reduction of 28.4 dB to that of the no-resonator complex beam in 140-160 Hz (see Fig. 9). That is, both the maximum and

average excited displacements the prescribed frequency range are reduced more than 28 times within the prescribed frequency range by the two optimization strategies. In addition, it also can be seen from Figs. 7 and 9 that different optimization strategies lead to beams with different dynamic properties. The optimal rainbow metamaterial beam by maximum-value based objective function has broader bandgap but bigger receptance value within the prescribed frequency range, which is contrary to the optimal beam derived by the average value based objective function. Optimization strategies can be selected according to requirements of specific applications.

Furthermore, the resonator distributions of two optimal rainbow metamaterial beams are also plotted in the subfigures of Figs. 7 and 9. Although the two beams have different resonator distributions, the total masses of their resonators are almost the same, e. g. with ratios of 10.5% and 10.4% to the mass of the Π-shaped beam with parallel plate insertions respectively.

5.2 Multi prescribed frequency range optimization

The prescribed multi-frequency ranges are assumed as 140~160 Hz and 410~430 Hz. Rainbow metamaterials with non-symmetric resonators are optimized to achieve good vibration attenuation inside these two frequency ranges. Weighted parameter of the two frequency ranges is set as $[0.5,0.5]^{T}$.

The maximum and average receptance value based objective functions defined by Eqs. (24) and (29) are utilized as two fitness functions respectively. The best fitness values of each generation during the GA optimization process are plotted in Figs. 10 and 12. As shown in Figs. 10 and 12, the best fitness values decrease gradually with the increase of generation, the vibration attenuation within the two frequency ranges are enlarged accordingly.

The optimal design variables by the maximal value based fitness function are

obtained as,

$$
\begin{aligned}
&m_{1i} = A_1 + B_1 \sin\left(C_1 x_{mi} + D_1\right) \quad i = 1, 2, ..., q \\
&A_1 = 0.056727\ m_r \\
&B_1 = 0.024099\ m_r \\
&C_1 = -1.51657 \\
&D_1 = 0.047384 \\
&m_{2i} = A_2 + B_2 \sin\left(C_2 x_{mi} + D_2\right) \quad i = 1, 2, ..., q \\
&A_2 = 0.053924\ m_r \\
&B_2 = 0.024125\ m_r \\
&C_2 = -0.93883 \\
&D_2 = -0.97644
\end{aligned}
\tag{32}
$$

While the optimal design variables obtained by the average value based objective function are

$$
\begin{aligned}
&m_{1i} = A_1 + B_1 \sin\left(C_1 x_{mi} + D_1\right) \quad i = 1, 2, ..., q \\
&A_1 = 0.052917\ m_r \\
&B_1 = 0.030663\ m_r \\
&C_1 = 0.14406 \\
&D_1 = 0.017146 \\
&m_{2i} = A_2 + B_2 \sin\left(C_2 x_{mi} + D_2\right) \quad i = 1, 2, ..., q \\
&A_2 = 0.030570\ m_r \\
&B_2 = 0.011427\ m_r \\
&C_2 = 0.30818 \\
&D_2 = 0.12283
\end{aligned}
\tag{33}
$$

The receptance values of the two optimal rainbow metamaterial beams are also compared with that of no-resonator complex beam of the same mass in Figs. 11 and 13. It can be seen that a bandgap emerges in each of the two optimization frequency ranges, therefore the vibration in both frequency ranges can be greatly attenuated. As shown in Fig. 11, the weighted maximum receptance value of the optimal beam by maximum value based objective function are 29 dB less than that of no-resonator complex beam of the same mass, which means the maximum vibration displacement is reduced 28 times inside the two optimization frequency ranges. Meanwhile, the optimal

metamaterial beam by average value based objective function has a weighted average value about 33 dB less than that of no-resonator beam of the same mass as shown in Fig. 13, therefore, the average displacement is shrunk by a factor of 45 within the two frequency ranges.

Besides, it can be seen from Figs. 11 and 13 that the optimal metamaterial beam obtained by maximum value based objective function has broader bandgaps and bigger receptance value than the other beam obtained by average value based objective function inside the prescribed two frequency ranges, which is identical to the comparison between the two beams optimized within single frequency range.

Moreover, although the different strategies could result in different optimal metamaterial beams, the two sets of resonators of the two optimal metamaterial beams have close total mass, with $\sum \mathbf{M}_1 \approx 5.3\% M$, $\sum \mathbf{M}_2 \approx 3.2\% M$ for both beams.

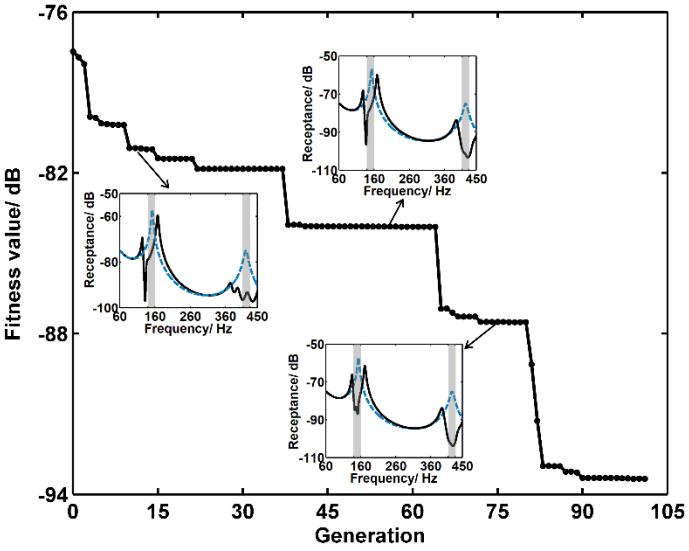

Fig. 10 The evalution history of the best fitness value of each generation during the multi-frequency range optimization process with the maximum receptance value based objective function. Receptance values comparison between three rainbow metamaterial beams (——) in the optimization process and no-resonator Π-shaped beams (- - -) of the same mass are shown in the three subfigures.

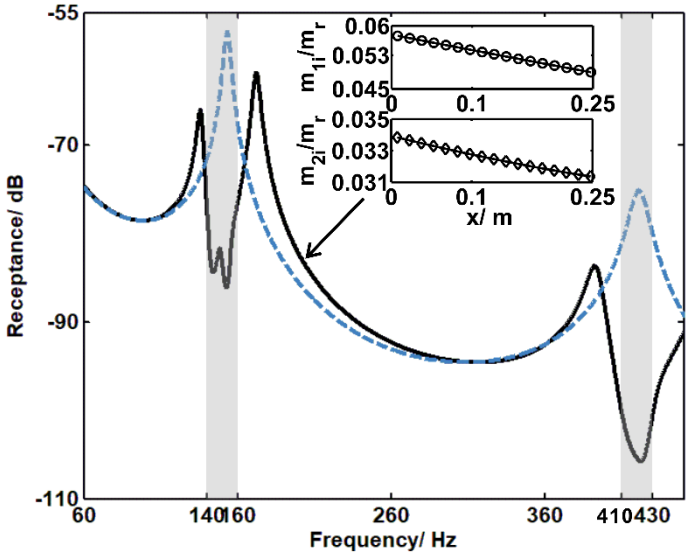

Fig. 11 Receptance value comparison between optimal rainbow metamaterial beam (——) by multi-frequency maximum receptance value based objective function and no-resonator Π-shaped beam (- - -) of the same mass. The resonator mass of the optimal beam is plotted in the subfigure.

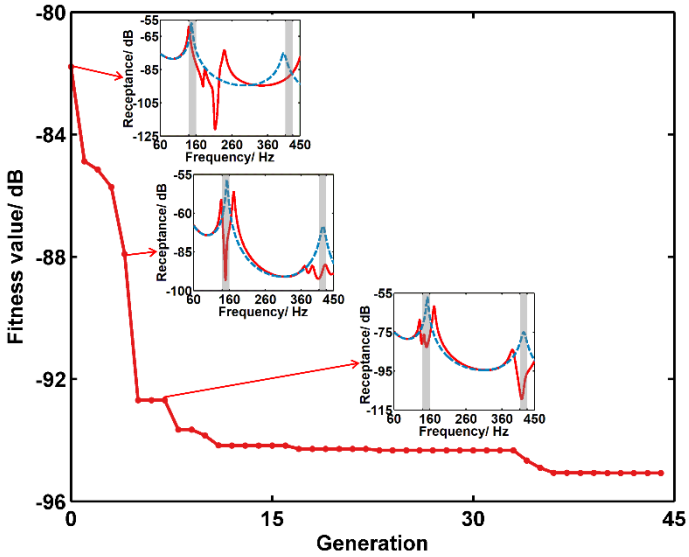

Fig. 12 The evalution history of the best fitness value of each generation during the multi-frequency range optimization process with the average receptance value based objective function. Receptance values comparison between three rainbow metamaterial beams (——) in the optimization process and no-resonator Π-shaped beams (- - -) of the same mass are shown in the three subfigures.

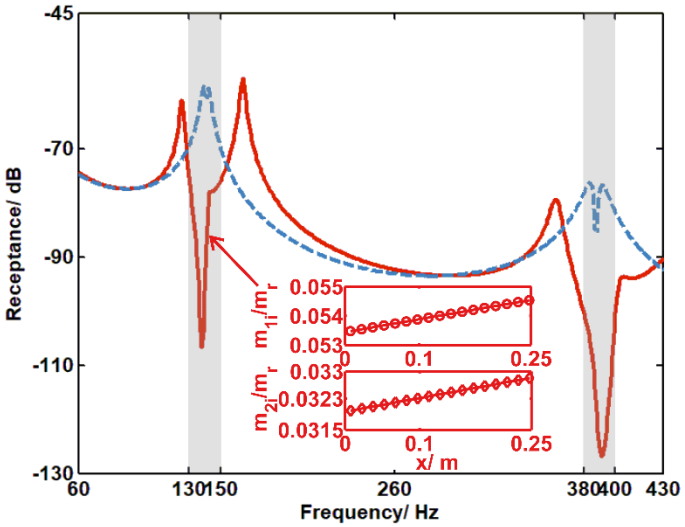

Fig. 13 Receptance value comparison between optimal rainbow metamaterial beam (——) by multi-frequency average receptance value based objective function and no-resonator Π-shaped beam (- - -) of the same mass. The resonator mass of the optimal beam is plotted in the subfigure.

6. Conclusions

In the present paper, optimization approaches were proposed for rainbow metamaterials which were composed of Π-shaped beams as backbones and two sets of nonperiodically distributed cantilever-mass resonators. FRFs of the rainbow metamaterials were first estimated by an analytical model which was then verified by experimental results. Two optimization strategies were subsequently devised to maximize the vibration attenuation within frequency ranges of interest on the basis of the analytical model, including minimizing the maximum and average receptance values. By carrying out dedicated optimization examples, it was found that optimal metamaterial beams obtained by both strategies could have dramatically reduced receptance values within the prescribed single and multiple frequency ranges compared with complex beams of the same mass. Besides, optimal beams by different optimization strategies exhibited different resonator distributions and hence various FRFs properties. The optimal beams with resonator distributions obtained by maximum

value based objective functions had wider bandgaps but weaker vibration attenuation in the prescribed frequency ranges than the optimal beams obtained by the average value based objective functions. Furthermore, although the optimal resonator distributions differ with optimization strategies, their total mass is fairly close.

The proposed design routes in the present paper can control the FRFs of the rainbow metamaterials at frequencies of interest accurately, hence help improve the applicability of the metamaterials for various applications. The rainbow metamaterials can not only be easily extended to industrial honeycomb composites that have found application in many industrial fields, the optimization scheme can act as a benchmark that inspires researchers in related areas to design various nonperiodic metamaterials with superior dynamic properties following the same procedures.

Acknowledgements

We would like to acknowledge the support acquired by the H2020 DiaMoND project [Grant Agreement ID:785859], Royal Society Grant: PURSUIT, the Brazilian National Council of Research CNPq [Grant Agreement ID: 420304/2018-5] and the Brazilian Federal District Research Foundation [Grant Agreement ID: 0193.001507/2017]. We also thank Waiel Elmadih for assistance in the FRF testing experiment.

References

[1] J.B. Pendry, Negative refraction makes a perfect lens. Phy Rev Lett, 2000;85: 3966-3969.

[2] J.B. Pendry, Negative refraction, Contemporary Physics, 45 (2004) 191-202.

[3] R.A. Shelby, D.R. Smith, S. Schultz, Experimental verification of a negative index of refraction. Science 2001;292:77-79.

[4] T. Tanaka, A. Ishikawa, S. Kawata, Unattenuated light transmission through the interface between two materials with different indices of refraction using magnetic

metamaterials. Phys Rev B 2006; 73:125423.

[5] A. Wang, A. Tuniz, P.G. Hunt, E.M. Pogson, R.A. Lewis, A. Bendavid, S.C. Fleming, B.T. Kuhlmey, M.C. Large, Fiber metamaterials with negative magnetic permeability in the terahertz. Opt Mater Express 2011;1:115-120.

[6] D. Schurig, J. Mock, D. Smith, Electric-field-coupled resonators for negative permittivity metamaterials. Appl Phys Lett 2006;88:041109.

[7] Z. Liu, X. Zhang, Y. Mao, Y. Zhu, Z. Yang, C.T. Chan, P. Sheng, Locally resonant sonic materials. Science 2000;289:1734-1736.

[8] S. Yao, X. Zhou, G. Hu, Experimental study on negative effective mass in a 1D mass–spring system. New J Phys 2008;10:043020.

[9] S. Yao, X. Zhou, G. Hu, Investigation of the negative-mass behaviors occurring below a cut-off frequency. New J Phys 2010;12:103025.

[10] M. Gao, Z. Wu, Z. Wen, Effective negative mass nonlinear acoustic metamaterial with pure cubic oscillator. Adv Civ Eng 2018;2018.

[11] H. H. Huang, C. T. Sun, Wave attenuation mechanism in an acoustic metamaterial with negative effective mass density. New J Phys 2009;11:013003.

[12] H. H. Huang, C. T. Sun, G. L. Huang, On the negative effective mass density in acoustic metamaterials. Int J Eng Sci 2009;47:610-617.

[13] N. Cselyuszka, M. Sečujski, V. Crnojević-Bengin, Novel negative mass density resonant metamaterial unit cell. Phys Lett A 2015;379:33-36.

[14] S. H. Lee, C. M. Park, Y. M. Seo, Z. G. Wang, C. K. Kim, Acoustic metamaterial with negative density. Phys Lett A 2009;373:4464-4469.

[15] Z. Yang, J. Mei, M. Yang, N. Chan, P. Sheng, Membrane-type acoustic metamaterial with negative dynamic mass. Phys Rev Lett 2008;101:204301.

[16] N. Fang, D. Xi, J. Xu, M. Ambati, W. Srituravanich, C. Sun, X. Zhang, Ultrasonic

metamaterials with negative modulus. Nat Mater 2006;5:452.

[17] C. Ding, L. Hao, X. Zhao, Two-dimensional acoustic metamaterial with negative modulus. J Appl Phys 2010;108:074911.

[18] S. H. Lee, C. M. Park, Y. M. Seo, Z. G. Wang, C. K. Kim, Acoustic metamaterial with negative modulus. J Phys-Condens Mat 2009;21:175704.

[19] X. N. Liu, G. K. Hu, G. L. Huang, C. T. Sun, An elastic metamaterial with simultaneously negative mass density and bulk modulus. Appl Phys Lett 2011;98: 251907.

[20] X. Wang, Dynamic behaviour of a metamaterial system with negative mass and modulus. Int J Solids and Struct 2014;51:1534-1541.

[21] Y. Ding, Z. Liu, C. Qiu, J. Shi, Metamaterial with simultaneously negative bulk modulus and mass density. Phys Rev Lett 2007;99:093904.

[22] S. H. Lee, C. M. Park, Y. M. Seo, Z. G. Wang, C. K. Kim, Composite acoustic medium with simultaneously negative density and modulus. Phys Rev Lett 2010;104: 054301.

[23] J.M. Manimala, C. Sun, Microstructural design studies for locally dissipative acoustic metamaterials. J Appl Phys, 2014;115:023518.

[24] Y.F. Wang, Y.S. Wang, V. Laude, Wave propagation in two-dimensional viscoelastic metamaterials. Phys Rev B, 2015;92:104110.

[25] M. Lewinska, V. Kouznetsova, J. van Dommelen, A. Krushynska, M. Geers, The attenuation performance of locally resonant acoustic metamaterials based on generalised viscoelastic modelling. Int J Solids Struct, 2017;126:163-174.

[26] A. Krushynska, V. Kouznetsova, M. Geers, Visco-elastic effects on wave dispersion in three-phase acoustic metamaterials. J Mech Phys Solids, 2016;96:29-47.

[27] X. Xiao, Z.C. He, E. Li, A.G. Cheng, Design multi-stopband laminate acoustic

metamaterials for structural-acoustic coupled system. Mech Syst Signal Pr, 2019;115:418-433.

[28] H. Zhang, Y. Xiao, J. Wen, D. Yu, X. Wen, Flexural wave band gaps in metamaterial beams with membrane-type resonators: theory and experiment. J Phys D: Appl Phys 2015;48:435305.

[29] M. Nouh, O. Aldraihem, A. Baz, Wave propagation in metamaterial plates with periodic local resonances. J Sound Vib 2015;341:53-73.

[30] C. Sugino, S. Leadenham, M. Ruzzene, A. Erturk, On the mechanism of bandgap formation in locally resonant finite elastic metamaterials. J Appl Phys 2016;120: 134501.

[31] D. Yu, Y. Liu, H. Zhao, G. Wang, J. Qiu, Flexural vibration band gaps in Euler-Bernoulli beams with locally resonant structures with two degrees of freedom. Phys Rev B 2006;73:064301.

[32] Y. Liu, D. Yu, L. Li, H. Zhao, J. Wen, X. Wen, Design guidelines for flexural wave attenuation of slender beams with local resonators. Phys Lett A 2007;362:344-347.

[33] Y. Li, L. Zhu, T. Chen, Plate-type elastic metamaterials for low-frequency broadband elastic wave attenuation. Ultrasonics 2017;73:34-42.

[34] S. Zhang, J. Hui Wu, Z. Hu, Low-frequency locally resonant band-gaps in phononic crystal plates with periodic spiral resonators. J Appl Phys 2013;113:163511.

[35] Y. Xiao, J. Wen, X. Wen, Flexural wave band gaps in locally resonant thin plates with periodically attached spring-mass resonators. J Phys D: Appl Phys 2012;45: 195401.

[36] H. Peng, P.F. Pai, H. Deng, Acoustic multi-stopband metamaterial plates design for broadband elastic wave absorption and vibration suppression. Int J Mech Sci 2015;103: 104-114.

[37] P. F. Pai, H. Peng, S. Jiang, Acoustic metamaterial beams based on multi-frequency vibration absorbers. Int J Mech Sci 2014;79:195-205.

[38] Z. Wang, P. Zhang, Y. Zhang, Locally resonant band gaps in flexural vibrations of a Timoshenko beam with periodically attached multioscillators. Math Probl Eng 2013;2013.

[39] R. Zhu, X. Liu, G. Hu, C. Sun, G. Huang, A chiral elastic metamaterial beam for broadband vibration suppression. J Sound Vib 2014;333:2759-2773.

[40] G. L. Huang, C. T. Sun, Band gaps in a multiresonator acoustic metamaterial. J Vib Acoust 2010;132:031003-031006.

[41] Y. Chen, M. Barnhart, J. Chen, G. Hu, C. Sun, G. Huang, Dissipative elastic metamaterials for broadband wave mitigation at subwavelength scale. Compos Struct 2016;136:358-371.

[42] Q. Q. Li, Z. C. He, E. Li, A. G. Cheng, Design and optimization of three-resonator locally resonant metamaterial for impact force mitigation. Smart Mater Struct 2018;27:095015.

[43] Q. Q. Li, Z. C. He, E. Li, A. G. Cheng, Improved impact responses of a honeycomb sandwich panel structure with internal resonators. Eng Optimiz 2019;1-21.

[44] Q. Q. Li, Z. C. He, E. Li, Dissipative multi-resonator acoustic metamaterials for impact force mitigation and collision energy absorption. Acta Mech 2019;230:2905-2935.

[45] Q. Q. Li, Z. C. He, E. Li, A. G. Cheng, Design of a multi-resonator metamaterial for mitigating impact force. J Appl Phys 2019;125:035104.

[46] H. Sun, X. Du, P. F. Pai, Theory of metamaterial beams for broadband vibration absorption. J Intel Mat Syst Struct 2010;21:1085-1101.

[47] P. F. Pai, Metamaterial-based broadband elastic wave absorber. J Intel Mat Syst

Struct 2010;21:517-528.

[48] H. W. Dong, S. D. Zhao, Y. S. Wang, C. Zhang, Topology optimization of anisotropic broadband double-negative elastic metamaterials. J Mech Phys Solids 2017;105:54-80.

[49] H. W. Dong, X. X. Su, Y. S. Wang, C. Zhang, Topological optimization of two-dimensional phononic crystals based on the finite element method and genetic algorithm. Struct Multidiscip Optim 2014;50:593-604.

[50] G. A. Gazonas, D. S. Weile, R. Wildman, A. Mohan, Genetic algorithm optimization of phononic bandgap structures. Int J Solids Struct 2006;43:5851-5866.

[51] D. Beli, A. T. Fabro, M. Ruzzene, J. R. F. Arruda, Wave attenuation and trapping in 3D printed cantilever-in-mass metamaterials with spatially correlated variability. Sci Rep 2019;9:5617.

Appendix

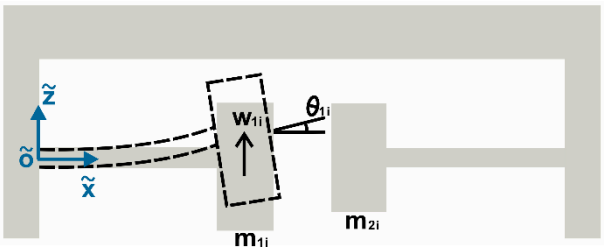

Fig. A1 Cross section of the Π-shaped beam with cantilever-mass resonators

For a slender cantilever beam clamped to the Π-shaped beam as shown in Fig. A1, the deflection of the cantilever beam can be written as

$$\delta_{1i}(\tilde{x})=Q_1 e^{-jk_{s1}\tilde{x}}+Q_2 e^{-k_{s1}\tilde{x}}+Q_3 e^{jk_{s1}\tilde{x}}+Q_4 e^{k_{s1}\tilde{x}}, \tag{A1}$$

where $k_{s1}=(\rho A_{s1}/EI_{s1})^{1/4}\sqrt{\omega}$, A_{s1} and I_{s1} are the cross section area and second moment of area of the cantilever beam respectively. ω denote the angular frequency. $(\tilde{x},\tilde{z})$ is the local coordinate on the cantilever-mass resonator as shown in Fig. A1.

Due to the clamped boundary condition, both the deflection and slope of the cantilever beam are zero at the interface of the Π-shaped beam and the cantilever beam,

$$\delta_{1i}\big|_{\tilde{x}=0} = 0 \tag{A2}$$

$$\delta'_{1i}\big|_{\tilde{x}=0} = 0 \ . \tag{A3}$$

At the other end of the cantilever beam, the displacement of the mass is governed by

$$m_{1i}\ddot{w}_{1i} = EI_{s1}\left.\frac{\partial^3 \delta_1}{\partial \tilde{x}^3}\right|_{\tilde{x}=l_{s1}} , \tag{A4}$$

where l_{s1} is the length of the cantilever beam, m_{1i} and w_{1i} represent the mass and its displacement in the ith segment of the Π-shaped beam respectively. The quantity w_{1i} is related to the deflection of the cantilever beam by

$$w_{1i} = \delta_{1i}\left(\tilde{x}\right)\big|_{\tilde{x}=l_{s1}} + W_{i,l}\big|_{x=x_i+p_iL_d} . \tag{A5}$$

In addition, the rotatory movement of the mass is governed by

$$EI_{s1}\,\delta''_{1i}\big|_{\tilde{x}=l_{s1}} + J_{1i}\ddot{\theta}_{1i} = 0 , \tag{A6}$$

where J_{1i} represents the moment of inertia of the mass, θ_{1i} denotes the rotation angle of the mass (see Fig. A1). Since the rotation angle of the mass is small, it can be approximated by

$$\theta_{1i} \approx \tan\theta_{1i} \approx \delta'_{1i}\big|_{\tilde{x}=l_{s1}} . \tag{A7}$$

Substituting Eq. (A7) into (A6), yields

$$EI_{s1}\,\delta''_{1i}\big|_{\tilde{x}=l_{s1}} - J_{1i}\omega^2\,\delta'_{1i}\big|_{\tilde{x}=l_{s1}} = 0 . \tag{A8}$$

Combing Eqs. (A2), (A3), (A4), (A8) with Eq. (A1), the unknown parameters are derived as

$$\left[Q_1, Q_2, Q_3, Q_4\right]^{\mathrm{T}} = \mathbf{T}_s^{-1}\left[0, 0, -m_{1i}\omega^2\, W_{i,l}\big|_{x=x_i+p_iL_d}, 0\right]^{\mathrm{T}} , \tag{A9}$$

where $\mathbf{T}_s$ is

$$\mathbf{T}_s=\begin{bmatrix} 1 & 1 & 1 & 1 \\ -\mathrm{j}k_{s1} & -k_{s1} & \mathrm{j}k_{s1} & k_{s1} \\ \begin{pmatrix}\mathrm{j}EI_{s1}k_{s1}^3\\ +m_{1i}\omega^2\end{pmatrix}\mathrm{e}^{-\mathrm{j}k_{s1}l_{s1}} & \begin{pmatrix}-EI_{s1}k_{s1}^3\\ +m_{1i}\omega^2\end{pmatrix}\mathrm{e}^{-k_{s1}l_{s1}} & \begin{pmatrix}-\mathrm{j}EI_{s1}k_{s1}^3\\ +m_{1i}\omega^2\end{pmatrix}\mathrm{e}^{\mathrm{j}k_{s1}l_{s1}} & \begin{pmatrix}EI_{s1}k_{s1}^3\\ +m_{1i}\omega^2\end{pmatrix}\mathrm{e}^{k_{s1}l_{s1}} \\ \begin{pmatrix}-EI_{s1}k_{s1}^2\\ +\mathrm{j}k_{s1}J_{1i}\omega^2\end{pmatrix}\mathrm{e}^{-\mathrm{j}k_{s1}l_{s1}} & \begin{pmatrix}EI_{s1}k_{s1}^2\\ +J_{1i}\omega^2k_{s1}\end{pmatrix}\mathrm{e}^{-k_{s1}l_{s1}} & \begin{pmatrix}-EI_{s1}k_{s1}^2\\ -\mathrm{j}k_{s1}J_{1i}\omega^2\end{pmatrix}\mathrm{e}^{\mathrm{j}k_{s1}l_{s1}} & \begin{pmatrix}EI_{s1}k_{s1}^2\\ -J_{1i}\omega^2k_{s1}\end{pmatrix}\mathrm{e}^{k_{s1}l_{s1}} \end{bmatrix}. \quad \text{(A10)}$$

The interaction force between the cantilever-mass resonator and the Π-shaped beam can be obtained based on Eqs. (A9) and (A1),

$$F_{1i}=-EI_{s1}\,\delta_{1i}'''\big|_{\tilde{x}=0}=N_{1i}\,W_{i,l}\big|_{x=x_{i-1}+p_iL_d}, \quad \text{(A11)}$$

where $N_{1i}=-EI_{s1}k_{s1}^3m_{1i}\omega^2\left(-\mathrm{j}\mathbf{T}_s^{-1}(1,3)+\mathbf{T}_s^{-1}(2,3)+\mathrm{j}\mathbf{T}_s^{-1}(3,3)-\mathbf{T}_s^{-1}(4,3)\right)$.

Therefore, the total interaction force $F_{i,t}$ between the Π-shaped beam and the two cantilever-mass resonators inside each substructure can be derived by the deflections of the two cantilever beams

$$F_i=F_{1i}+F_{2i}, \quad \text{(A12)}$$

where F_{2i} is the interaction force between the other mass m_{2i} and Π-shaped beam which can be figured out by following the same calculation method of F_{1i}.